Interfacial Bonding Controls Friction in Diamond–Rock Contacts

Journal:	*The Journal of Physical Chemistry*
Manuscript ID	jp-2021-02857v.R2
Manuscript Type:	Article
Date Submitted by the Author:	n/a
Complete List of Authors:	Bhamra, Jagjeevan; Imperial College London, Mechanical Engineering Ewen, James; Imperial College London, Mechanical Engineering Ayestaran Latorre, Carlos; Imperial College London Bomidi, John; Baker Hughes Inc Bird, Marc; Baker Hughes Inc Dasgupta, Nabankur; Pennsylvania State University, Engineering Science and Mechanics van Duin, Adri; Pennsylvania State University, Mechanical and Nuclear Engineering Dini, Daniele; Imperial College London, Mechanical Engineering

Interfacial Bonding Controls Friction in Diamond—Rock Contacts

Jagjeevan S. Bhamra,[1] James P. Ewen,[1,2,3,*] Carlos Ayestarán Latorre,[1,4] John A. R. Bomidi,[5] Marc W. Bird,[5] Nabankur Dasgupta,[6] Adri C. T. van Duin,[6,7] and Daniele Dini[1,2,3]

[1] – Department of Mechanical Engineering, Imperial College London, South Kensington Campus, London, SW7 2AZ, U.K.

[2] – Institute of Molecular Science and Engineering, Imperial College London, South Kensington Campus, London, SW7 2AZ, U.K.

[3] – Thomas Young Centre for Theory and Simulation of Materials, Imperial College London, South Kensington Campus, London, SW7 2AZ, U.K.

[4] – Department of Materials, Imperial College London, South Kensington Campus, London, SW7 2AZ, U.K.

[5] – Baker Hughes Inc., Center for Technology Innovation, Houston, Texas 77040, U.S.A.

[6] – Department of Engineering Science and Mechanics, The Pennsylvania State University, University Park, Pennsylvania 16802, U.S.A.

[7] – Department of Mechanical Engineering, The Pennsylvania State University, University Park, Pennsylvania 16802, U.S.A.

* – Corresponding author email: j.ewen@imperial.ac.uk

Abstract

Understanding friction at diamond–rock interfaces is crucial to increase the energy efficiency of drilling operations. Harder rocks usually are usually more difficult to drill; however, poor performance is often observed for polycrystalline diamond compact (PDC) bits on soft calcite-containing rocks, such as limestone. Using macroscale tribometer experiments with a diamond tip, we show that soft limestone rock (mostly calcite) gives much higher friction coefficients compared to hard granite (mostly quartz) in both humid air and aqueous environments. To uncover the physicochemical mechanisms that lead to higher kinetic friction at the diamond–calcite interface, we employ nonequilibrium molecular dynamics simulations (NEMD) with newly developed Reactive Force Field (ReaxFF) parameters. In the NEMD simulations, higher friction coefficients are observed for calcite than quartz when water molecules are included at the diamond–rock interface. We show that the higher friction in water-lubricated diamond–calcite than diamond–quartz interfaces is due to increased interfacial bonding in the former. For diamond–calcite, the interfacial bonds mostly form through chemisorbed water molecules trapped between the tip and the substrate, while mainly direct tip-surface bonds form inside diamond–quartz contacts. For both rock types, the rate of interfacial bond formation increases exponentially with pressure, which is indicative of a stress-augmented thermally activated process. The mean friction force is shown to be linearly dependant on the mean number of interfacial bonds during steady-state sliding. The agreement between the friction behaviour observed in the NEMD simulations and tribometer experiments suggests that interfacial bonding also controls diamond–rock friction at the macroscale. We anticipate that the improved fundamental understanding provided by this study will assist in the development of bit materials and coatings to minimise friction by reducing diamond–rock interfacial bonding.

Introduction

The underlying physicochemical mechanisms that control friction between sliding surfaces remain poorly understood. In some systems, friction can be described through the dynamical formation and rupture of interfacial bonds.[1] Filippov et al.[2] developed a model that directly relates macroscopic friction to the formation and rupture dynamics of interfacial molecular bonds. Using nonequilibrium molecular dynamics (NEMD) simulations of hydrogen-terminated amorphous carbon atomic force microscopy (AFM) tips and diamond substrates, Mo et al.[3] showed that the kinetic friction force depended linearly on the number of atoms that chemically interact across the sliding contact. Subsequent AFM experiments by Li et al.[4] revealed that interfacial bonds also control static friction in silica–silica contacts. They suggested that the large amount of interfacial bonding at the nanoscale is quantitatively consistent with that

required to explain the frictional aging phenomena,[4] which is commonly observed in macroscale rock friction experiments.[5] Interfacial bonding could also be an important factor in controlling the friction of rocks with other materials, such as diamond drill bits.

Rock drilling is a crucial process for many areas of the energy industry, from the extraction of oil and gas[6] to the utilisation of geothermal energy.[7] Over the next decade, drilling could also play a central role to facilitate carbon capture and storage[8] and the safe disposal of radioactive waste.[9] Recent estimates have suggested that, in the energy industry, friction and wear account for around 40 % of total energy losses.[10] A significant proportion of these losses originate from the drilling of rocks, which is a rather inefficient process. Drilling efficiency is usually defined as the ratio of the rock compressive strength to the mechanical specific energy.[11] At high cutting depths, the drilling efficiency is between 30–50 %, although this can be as low at 10 % at low cutting depths, where most of the energy dissipation occurs through frictional contact.[12] Drilling efficiency could be improved through the development of improved bit materials and coatings.[13] This could also improve the economic feasibility of deep-well drilling (below 1.5 km), which would be beneficial for oil, gas, and particularly geothermal applications.[14] The cost of wells increases almost exponentially with increasing depth[14] and drilling costs average 50 % of the $3–8M total cost of deep wells.[15]

The introduction of polycrystalline diamond compact (PDC) bits during the 1970s[16] was a significant advancement in drilling technology.[17] PDC bits proved to be extremely effective in drilling soft to medium rock formations (e.g. clay, sand, shale, limestone, sandstone, and siltstone), where they achieved high rates of penetration (ROP) while also maintaining long bit life.[17] However, in harder formations (e.g. mudstone, chert, pyrite, granite, and quartzite), both ROP and bit life were substantially reduced.[17] The ROP is reduced by high friction coefficients at the bit–rock interface, which are 3–5 times higher for PDCs compared to other (roller cone, tungsten carbide insert) drill bits.[18] High friction coefficients, coupled with high sliding velocities (> 1 m s^{-1}),[19] result in large temperature rises (hundreds of degrees) at the bit–rock interface,[19] which can promote deleterious structural transformations (graphitisation) within the surfaces of PDC bits.[20,21] These transformations, coupled with increased abrasive wear due to the higher hardness of the counter surface,[22] are the principal causes of reduced bit life in hard rock formations.

Ersoy and Waller suggested that the majority of damage to PDC bits was due to abrasive wear.[23] In fact, abrasive wear is the major wear mechanism in most tribological systems.[22] The Archard equation[24] is the most popular empirical model to predict abrasive wear inside macroscale contacts:[25]

$$V = (K_b F_n d)/H \quad (1)$$

where V is the wear volume, K_b is the wear coefficient, F_n is the load, d is the sliding distance, and H is hardness. The Archard equation[24] has frequently been used to model the abrasive wear of PDC bits.[26–28] The hardness of the polycrystalline diamond (PCD) used in PDC bits is at least 55 GPa.[19] During the drilling process, the bits can often pass through greatly varying geologies. Even within a single rock type, the properties can vary markedly and can be heterogeneous and scale-dependant. Mean hardness values have been measured for several rock types, for example, calcite-rich rocks (e.g. limestone) have mean hardness of ~2 GPa, while quartz-rich rocks (e.g. granite) have a mean hardness of 9–15 GPa.[19,29] Since these are both much softer than PCD under ambient or typical wellbore temperatures (< 300 °C), low abrasive wear rates are expected from the Archard model[24] for PDCs when drilling both granite and particularly limestone rocks. However, the effective hardness of PCD can be reduced below that of quartz (but not calcite) when local cutting temperatures exceed ~750 °C.[30] Under these accommodating conditions, PDCs are susceptible to abrasive wear.[31] This is consistent with experimental observations of higher PDC wear when drilling granite compared to limestone.[23]

As in many tribological systems involving direct solid-solid contact,[32] stick-slip can occur during PDC drilling.[33–35] During drilling operations, PDCs can periodically stop and then rapidly accelerate to velocities that are 2–3 times the applied velocity.[34] This is highly undesirable since it leads to vibrations that can reduce both ROP and bit life.[35] Stick-slip behaviour is particularly prevalent at low rotation speed (sliding velocity) and high weight-on-bit (pressure) conditions.[34] It is now widely accepted that bit–rock interactions are critical to the oscillatory friction and stick-slip behaviour observed when using PDCs.[33–35] Stick-slip is a particular problem in calcite-containing rocks (e.g. limestone) formations,[36] where rock powder has been observed to strongly adhere to the PDC surface following tribometer experiments.[37] These observations suggest that stick-slip could be caused by the cooperative rupture of chemical bonds at the sliding bit–rock interface.[2] Such behaviour has previously been confirmed in atomic force microscopy (AFM) experiments of sliding silica-silica interfaces.[4,38] Conversely, for quartz-containing rocks (e.g. granite), adhesion between the tip and rock are negligible, meaning that stick-slip is less problematic. The chemistry of the diamond–quartz interface is similar to that studied in previous experiments of silica AFM tips sliding on hydrogenated diamond substrates, on which stick-slip was found to be much less pronounced than for silica-silica interfaces.[4]

In addition to the development of new bit materials, drilling fluids can also be used to increase performance. Rehbinder showed that the addition of surfactants to circulating fluids could markedly influence the ROP in hard rocks.[39] The original mechanism offered by Rehbinder was that changes in drilling performance in different environments could be a consequence of adsorption-induced reduction in surface energy of the solid being penetrated.[40] Subsequently, Mills and Westwood,[41] suggested that surfactant solutions that increased the hardness of the rock surface could reduce the ploughing contribution to diamond–rock friction and thus also decrease frictional heating. Since higher temperatures result in increased wear, they suggested that solutions that increase rock surface hardness could reduce tip wear.[41] This is the opposite trend than would be predicted using the Archard abrasive wear model.[24] In more recent work by the same authors, the influence of several other factors, such as adsorption kinetics, polarity, and surfactant concentration, on bit wear were also considered.[42] Controversy still remains in this area due to the complex interacting processes involved in controlling drilling performance.[43] The physicochemical nature of these interactions and their effects on friction for different rock types remain unclear. One likely mechanism is that the surfactants reduce friction by passivating the sliding bit and rock surfaces and minimise interfacial bonding.

Macroscale numerical[44] and analytical[45] modelling techniques are commonly used to investigate friction at PDC bit–rock interfaces. However, these techniques are not capable of describing the physiochemical transformations that appear to control the tribological response of the system. NEMD simulations are becoming an increasingly useful tool to study physiochemical transformations inside tribological systems.[46] Following the seminal work of Mo et al.[3], NEMD simulations have been used to study the effect of interfacial bonding on friction in other systems. For example, NEMD simulations of the silica-silica interface using ReaxFF showed that friction increased due to the formation of interfacial siloxane (Si–O–Si) bridges between the sliding surfaces.[47] Similarly, NEMD simulations using density-functional-based tight binding (DFTB) indicated that interfacial C–C bonds increased the friction between sliding diamond-like carbon (DLC) surfaces.[48] However, NEMD simulations have not yet been used to study the diamond–rock interfaces relevant to PDC friction.

In this study, we use macroscale tribometer experiments and NEMD simulations to compare the kinetic friction of PDC bits on granite and limestone surfaces. In order to incorporate the effects of interfacial bonding, we employ the reactive force field (ReaxFF) method.[49] The computational cost of ReaxFF simulations are several orders of magnitude lower than first principles techniques, allowing much larger time and length scales to be accessed.[50] Unlike first-principles methods, careful parameterisation is required in order to obtain reliable results.

Over the last two decades, ReaxFF parameters have been developed to study a very wide range of systems and processes.[51] Of particular interest to this study, ReaxFF has been widely applied to study tribochemical processes occurring between sliding surfaces.[52] We employ published ReaxFF parameters for quartz[53] and develop new parameters for calcite. The tribometer experiments show that friction is much higher for diamond–limestone than diamond–granite interfaces under air and aqueous environments. The NEMD simulations show that this is due to increased interfacial bonding in diamond–calcite contacts during sliding, mostly through chemisorbed water molecules.

Methodology

Experimental Procedure

We used a pin-on-disk rotary tribometer for the friction measurements. Previous studies[54] have shown that the friction obtained in these experiments can be directly related to ROP in industry-standard tests such as the vertical turret lathe[17] and the ultra-deep single-cutter drilling simulator.[15] Sliding contact, as studied in these experiments, is experienced by worn and shaped cutting elements that are used in some rock drilling designs. In those elements, wherein the cutting action (indentation depth) is low, interfacial friction dominates the overall energy losses.

Carthage Limestone and Sierra White Granite cores were respectively chosen as representative limestone and granite rock types. The rock samples were all ground to the same smooth surface finish prior to the tribometer experiments ($R_q \approx 12$ μm).[55] Hemispherical PDC pins with a radius of 4.765 mm were employed, providing idealized point contacts. The root-mean-square surface roughness of the pins was measured using white light interferometry (R_a = 2.86 μm, R_q = 3.65 μm).[27,37] The tests were conducted in both aqueous and air environments (average relative humidity = 70 %). The experimental sliding velocity was 0.1 m s^{-1}, which is somewhat lower than that used in operational PDC drills (2–4 m s^{-1}).[19] The load was progressively increased (1–200 N) and held for 5 minutes at the same sliding velocity while friction data was measured. The maximum Hertz pressure, P_{max}, is approximately 2.5 GPa for limestone (F_n = 100 N) and 3.3 GPa for granite (F_n = 200 N). Due to the presence of roughness on the rock and diamond surfaces, the peak asperity pressures will be somewhat higher that predicted by the Hertz equation. However, the non-dimensional α parameters calculated for these systems (0.01–0.03) suggest that Hertz theory provides a reasonable estimate of the contact pressure (within 5 %).[56]

The velocities and loads were selected to characterize the friction response at sliding-dominated regimes, where the cutting action is relatively low. This ensured that the friction

forces measured were due mainly to interfacial interactions, rather than ploughing. In addition to the friction measurements, both rock and diamond surfaces were examined using optical microscopy following the tests. No wear of the tips was measurable following the tribometer experiments.

Simulation Setup

In the experiments, the mineral distribution within the granite and limestone rock substrates display spatial heterogeneity, resulting in location-dependant surface chemistry.[57] Due to their large computational expense,[50] NEMD simulations with ReaxFF are limited to the study of nanoscale systems.[46] Therefore, the major constituents of granite (quartz)[58] and limestone[59] (calcite) were used as representative models of the rock substrates. The suitability of this comparison was confirmed by energy-dispersive x-ray spectroscopy analysis of the transfer film on the diamond pin after the tribometer experiments (Figure S1). The atomically-smooth α-quartz{0001}[60] and calcite{10.4}[61] surfaces were selected, which have shown to be the most thermodynamically stable in previous density functional theory (DFT) studies.

Experimental evidence suggests that both quartz[62] and calcite[63] surfaces are hygroscopic and are likely to be covered by a water monolayer in both air and aqueous environments. Therefore, as well as the dry surfaces, we performed NEMD simulations using different numbers of water molecules to simulate humid air and aqueous environments. The NEMD simulations of the water-containing systems are expected to be more representative of the conditions in our tribology experiments and for operational PDCs. For the smaller number of water molecules (50), representing the air environment, the surfaces are covered by a water monolayer and most of the molecules remained chemisorbed to the surface during the equilibration phase. For the larger number of water molecules (150), representing the aqueous environment, there were additional water molecules on top of the complete water monolayer, which submerged the tip during sliding. As expected from previous DFT calculations, adsorbed water molecules spontaneously dissociate on both α-quartz{0001}[64] and calcite{10.4}[61] to form surface hydroxyl groups (Figure S2).

The tip was modelled by a single-crystal diamond hemisphere with a radius of 2.0 nm.[65] A representative system for the NEMD simulations (calcite surface with 150 water molecules) is shown in Figure 1. The tip radius is more than two orders of magnitude smaller than the experimental tip radius (4.765 mm), resulting in a much lower contact area, A_c. This is not expected to significantly affect the friction coefficient, however, since the load is reduced accordingly to approximately match the mean Hertz pressure for point contacts. Previous

studies have shown that the shear stress ($\tau = F_f / A_c$) at diamond–quartz interfaces is independent of both tip radius and tip geometry.[66]

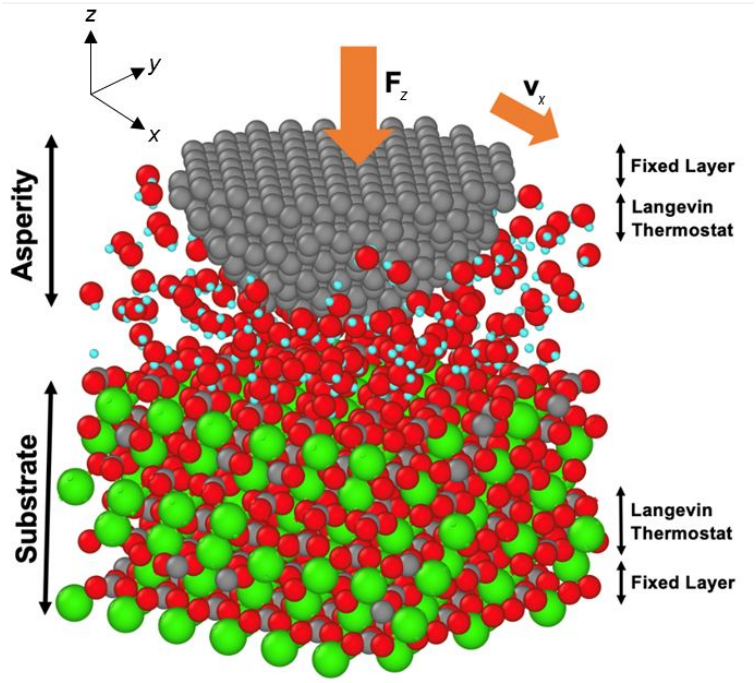

Figure 1. Representative system (calcite surface with 150 water molecules) for the NEMD simulations shown before equilibration. Calcium atoms are shown in green, carbon in grey, oxygen in red, and hydrogen in light blue. Rendered using OVITO.[67]

ReaxFF parameters

ReaxFF is a bond order-based force field that was originally developed by van Duin et al.[49] to study the reactivity of hydrocarbons. The version of ReaxFF implemented in LAMMPS uses the functional form that was originally outlined by Chenoweth et al.[68] and was described in more detail by Aktulga et al.[69] The general functional form of ReaxFF is given by:[51]

$$E_{system} = E_{bond} + E_{over} + E_{angle} + E_{tors} + E_{vdW} + E_{Coulomb} + E_{specific} \quad (2)$$

where E_{bond} is a continuous function of interatomic distance, describing the energy associated with bond formation (including σ, π, and π-π contributions). E_{angle} and E_{tors} are the energies associated with three-body angle and four-body torsional angle strain respectively. E_{over} is an energy penalty to prevent over-coordination of atoms and is based on atomic valence rules. $E_{Coulomb}$ and E_{vdW} represent the electrostatic and dispersive interactions between all atoms in the system, irrespective of their connectivity and bond order. $E_{specific}$ represents system-specific terms required to capture properties particular to the system of interest, such as lone-

pairs, conjugation, and hydrogen bonding.[51] The point charges on the atoms vary dynamically during the NEMD simulations and are calculated using the charge equilibration (Qeq) method.[69–71]

For the α-quartz{0001} surfaces, we use the Si/O/H/C ReaxFF parameters developed by Newsome et al.[53] to study the oxidation of silicon carbide by oxygen and water. This used a training set including previous first-principles data for silicon,[72] silicon oxides,[73,74] and polydimethylsiloxide.[75] The parameterisation accurately reproduces the experimental density and bulk moduli of α-quartz.[73] The relevant parameters have also been validated against first-principles methods for the interactions between silica surfaces and water molecules.[74] The parameters[53] have recently been successfully applied to study the adhesion between graphene sheets and amorphous silica substrates.[76]

A ReaxFF parameterisation is available that includes parameters for all of the elements of interest in this study.[77] Although this includes parameters developed for CaO,[78] $CaCO_3$ was not included in the training set and it performs poorly for this purpose.[79] A previous version included parameters for $CaCO_3$, but this required Ca atoms to be fixed as di-cations.[80] Therefore, in this study we developed new ReaxFF parameters for Ca/O/H/C using DFT that do not require fixed charges.

The DFT calculations of $CaCO_3$ were performed with the Jaguar software[81] using the M06-2x functional[82] with the LACV3P++** basis set. Full geometry optimizations were performed on these clusters without using any symmetry or structural constraints. To obtain potential energy profiles, constrained geometry optimization was applied for the Ca–O–C angle (65–130°) and the Ca–C off-diagonal (1.0–4.2 Å). The vibrational frequency of $CaCO_3$ was also calculated using the same functional and basis set.

Periodic DFT calculations for $CaCO_3$ and Ca condensed phases were then performed using the Vienna ab initio simulation package (VASP).[83–85] The DFT calculations use projector augmented wave (PAW) pseudopotentials[86] and Perdew-Burke-Ernzerhof (PBE) exchange-correlation functional[87] with an energy cutoff of 520 eV. All calculations were performed using spin polarization. For $CaCO_3$, the Brillouin zone is sampled with an (4 × 4 × 4) Monkhorst-Pack k-point mesh.[88] The equilibrium lattice constant was calculated and the equation of state was determined by deforming the lattice by ±10 %.

In this study, we have optimized the ReaxFF parameters for the Ca–O–C angle and the Ca–C off-diagonal to develop a transferable ReaxFF potential for Ca/C/O interactions, without

requiring local charge constraints.[80] The Ca–O parameters were obtained from Pitman and van Duin.[77] The interaction between calcite surfaces and water molecules has previously been validated against first-principles calculations[80] and the relevant parameters remain unchanged here. The new parameters were developed by training against new and existing DFT data. We used the standard ReaxFF parameter optimization strategy, which involves a weighted single-parameter search method.[51] Parameter correlations, which are quite extensive in ReaxFF, are captured by performing multiple loops over the optimizable force field parameters until the force field error converges. The weights depend on the relevance of a particular training set data point; in general, data points closer to the equilibrium were given higher weights.

Figure 2 shows the comparison between ReaxFF and the DFT energies for the Ca–O–C angle (a) the Ca–C off-diagonal (b) scanning. The agreement between ReaxFF and DFT is relatively good; most of the energy differences are comparable to the typical error of DFT calculations. The mean energy deviation of ReaxFF is 5.2 kcal mol^{-1} for the Ca–O–C angle and 7.5 kcal mol^{-1} for the Ca–C off-diagonal. The vibrational frequencies of $CaCO_3$ obtained with DFT and ReaxFF are also in good agreement (Figure S3 and Figure S4).

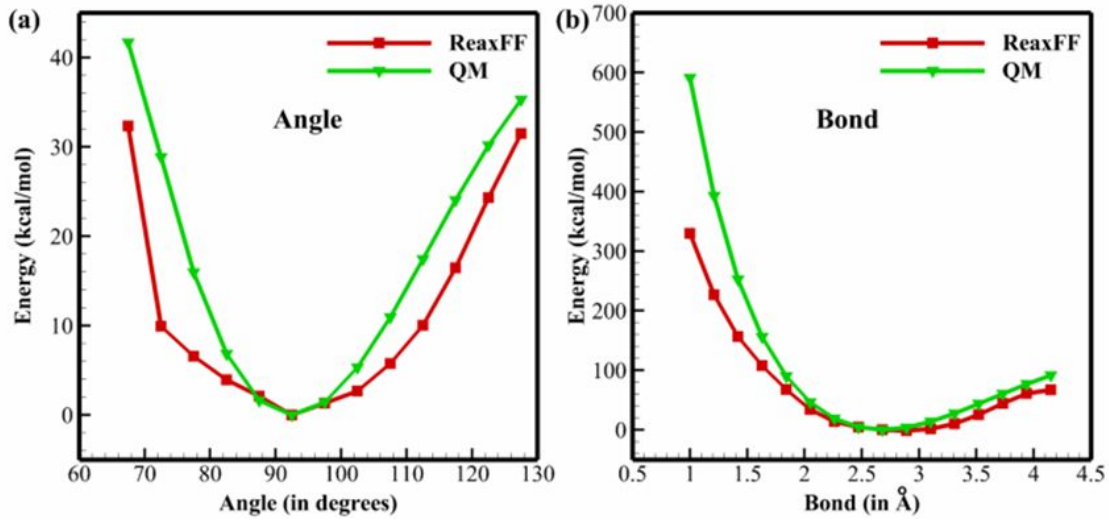

Figure 2. Comparisons of energy from ReaxFF (red) and DFT (green) for constraining of (a) Ca–O–C angle and (b) Ca–C off-diagonal.

The training set also included condensed phase data for the equation of state for the condensed calcite phase of $CaCO_3$. ReaxFF was trained against the difference in energy when the volume was varied from ±10 % of the equilibrium value, as shown in Figure 3. The ReaxFF parameterisation reproduced the equilibrium density of calcite from DFT within the uncertainty of the measurements, but it slightly underestimates the volume-energy curvature

close to the equilibrium density. The heat of formation and heat of reaction of calcite were also included within the training set. The ReaxFF parameters provides similar energy values for these reactions as the DFT calculations (Table S1).

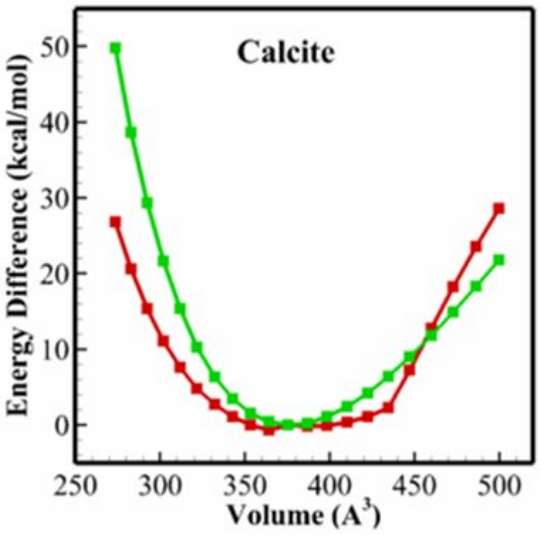

Figure 3. Equations of state of calcite from ReaxFF (red) and DFT (green).

Simulation Details

We performed NEMD simulations using the large atomic/molecular massively parallel simulator (LAMMPS) software package.[89] We used the velocity-Verlet integration algorithm[90] with a time step of 0.25 fs. The bottom atomic layer of the substrate was frozen, and periodic boundary conditions were applied in the *x*- and *y*-directions. The temperature was maintained at 300 K using a Langevin thermostat with a coupling time of 25 fs. The thermostat was only applied to the central layers (in the *z*-direction) of the tip and substrate, as shown in Figure 1. A reflective boundary was added in the *xy*-plane at the top of the simulation cell to prevent desorbed species from escaping.

The systems were energy minimised, before being equilibrated at 300 K for 0.1 ns. During the equilibration, a constant normal force (F_n = 0.1 nN) was added to the outer layer of atoms in the tip to bring it in contact with the substrate. The normal force was then increased to the target value (F_n = 2.5–40 nN) and the tip was given a sliding velocity in the *x*-direction (v_x = 10 m s^{-1}). This resulted in maximum Hertz pressures in the range P_{max} = 1.9–3.9 GPa for diamond–calcite and P_{max} = 2.0–4.1 GPa for diamond–quartz. We found that there was negligible difference in the change in friction force with sliding distance for sliding velocities between 1 m s^{-1} and 10 m s^{-1} (Figure S5). Therefore, to reduce the computational expense, all results discussed from this point onwards refer to a tip sliding velocity of 10 m s^{-1}. The sliding

simulations were performed for 0.75 ns, which was sufficient for the friction force and number of interfacial bonds to reach a steady state. Chemical bonding information was output every 1.0 ps, using a bond order cutoff of 0.3 to identify covalent bonds.[68] The choice of bond order cutoff only affects the post-processing analysis and does not influence the ReaxFF energy or force calculations.[77,91]

Results and Discussion

Tribometer Experiments

First, we studied the variation in the friction force, F_f, with normal force, F_n, using macroscale tribometer experiments (Figure 4) with diamond–granite (black) and diamond–limestone (red) point contacts in a humid air environment. For both rock types, the friction force increases roughly linearly with normal force with a near-zero intercept. This is consistent with Amontons' friction equation, which states that the coefficient of friction (COF), $\mu = F_f/F_n$. Such a relationship is expected in macroscale contacts and is usually attributed to a linear increase in real contact area between randomly rough surfaces.[3] The linear fits in Figure 4 yield μ = 0.38 for diamond–limestone and μ = 0.18 for diamond–granite in an air environment. For the diamond–granite contact, the intercept of the linear fit had an intercept of 4 N, suggesting some adhesion at the interface.[3]

We obtained similar results in an aqueous environment, but with a slightly higher (~10 %) friction coefficient for both rock types. Previous studies have shown that humidity can significantly affect rock friction.[92] In the current experiments, the air relative humidity (70 %) is already sufficiently high such that there was only a slight increase in friction when changing to an aqueous environment. After the friction experiments, we observed that limestone powder strongly adhered to the diamond tip (Figure S1), which has previously been noted for PDCs that have been used to drill calcite-containing rocks.[37]

The friction–load curves in Figure 4 are slightly sigmoidal, particularly for the diamond–limestone contact. At low load (F_n < 80 N), F_f increases sublinearly with F_n, which is consistent with Hertz theory ($F_f \propto F_n^{2/3}$),[3] as shown by the dotted lines in Figure 4. At higher loads (F_n < 80 N), F_f increases superlinearly with F_n, which implies that the interfacial shear strength increases markedly above a critical load, corresponding to a maximum Hertz pressure of around 2 GPa. While many multi-asperity theories of rough contact predict a linear increase in F_f with F_n,[3] they cannot explain the superlinear increase seen in Figure 4. We attribute the superlinear increase of F_f with F_n at high load to interfacial bond formation, as predicted by the interfacial bonding friction model developed by Filippov et al.[2]. The larger stresses

encountered at higher load increase the probability for interfacial bond formation by decreasing the activation energy.[93] The formation of a greater number of interfacial bonds at high load, which must be ruptured for sliding to proceed, leads to higher friction than is predicted by contact mechanics theories.[93] Superlinear friction–load behaviour has recently been observed in AFM experiments of silica–silica contacts,[94] which are known to form interfacial bonds.[4] In summary, diamond–rock friction can be adequately described by contact mechanics theories up to a critical load (or pressure) above which interfacial bonding occurs, leading to much higher friction than would otherwise be expected. The friction–load behaviour is more sigmoidal for diamond–calcite than diamond–quartz contacts, suggesting stronger interfacial bonding for the former. The relationship between interfacial bonding and friction was quantified and analysed using NEMD simulations.

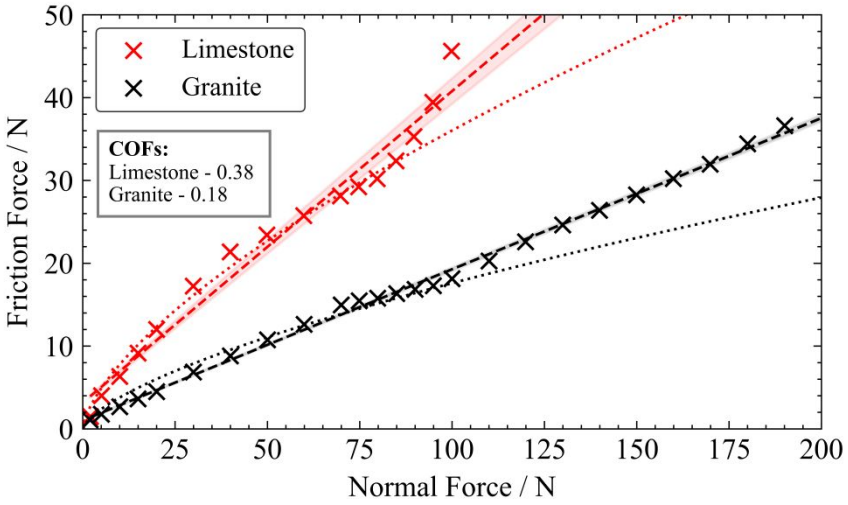

Figure 4. Variation in the friction force, F_f, with normal force, F_n, from the macroscale tribometer experiments with diamond–granite (black) and diamond–limestone (red) point contacts in an air environment. Dashed lines are linear fits to Amontons' friction equation. Shaded regions represent 95 % confidence intervals. Dotted lines are estimates for the low-load region (< 80 N) based on Hertz theory ($F_f \propto F_n^{2/3}$).[3]

NEMD Simulations

Figure 5 shows how the friction force, F_f, changes with sliding time in the NEMD simulations. The friction force generally increases at short sliding times (< 200 ps) before reaching a steady state. For the water-containing diamond–quartz systems (Figures 5b and 5c), the friction force reaches a maximum before reducing to the steady-state value. Friction curves with similar shapes has been observed previously in NEMD simulations of silica–silica interfaces[47] and tribometer experiments of quartz-containing sandstone rocks.[95] For a subset of systems, longer simulations were performed in which there was no further change to the mean friction

force. The steady-state friction force values shown from this point onwards are averaged over the final 200 ps of sliding. Stick-slip friction is observed for all of the studied systems. The degree of stick-slip is more severe in the absence of water (Figure 5a) than when it is present (Figures 5b and 5c), but is quite similar for the quartz and calcite substrates.

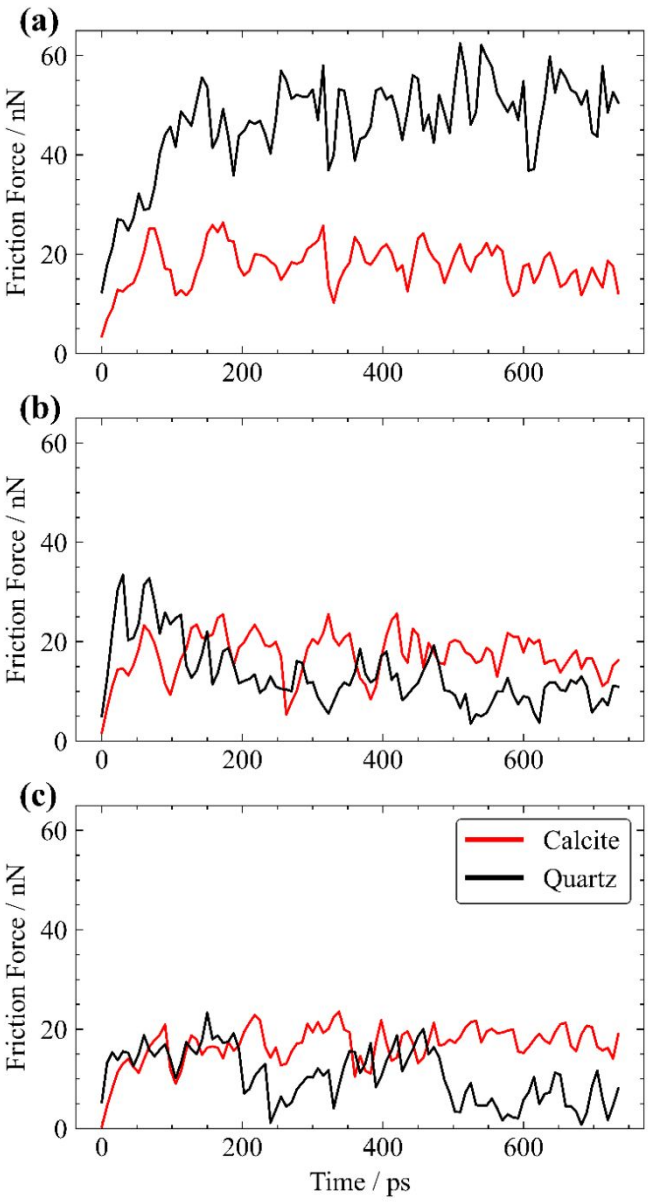

Figure 5. Variation in friction force, F_f, with sliding time from the NEMD simulations for diamond–quartz (black) and diamond–calcite (red) interfaces with 0 (a), 50 (b), and 150 (c) water molecules. Normal force, F_n = 35 nN, sliding velocity, v_x = 10 m s^{-1}.

Figure 6 shows that F_f increases approximately linearly with F_n in all of the NEMD simulations. This is in agreement with the experimental friction results (Figure 4) and is consistent with Amontons' equation.[3] Given that a point contact geometry was used in the simulations, one

might expect that $F_f \propto F_n^{2/3}$, which is consistent with Hertz theory.[3] The linear increase in F_f with F_n observed in Figure 6 indicates that the interfacial shear strength increases with pressure,[3] which we attribute to interfacial bond formation. The water-lubricated diamond–calcite contacts (Figure 6b and Figure 6c) show a superlinear increase of F_f with F_n at low loads, which can be explained by stress-assisted interfacial bonding.[93] It is noteworthy that this behaviour occurs at a similar pressure (2 GPa) as in the experiments (Figure 4). The water-lubricated diamond–granite contacts show a more linear increase in F_f with F_n, which suggests that interfacial bond formation is less prolific compared to diamond–calcite interfaces. Previous single-asperity AFM friction measurements of silica–silica contacts (in which interfacial bonds are known to form[4]) have shown both linear[96] and superlinear[94] increases in F_f with F_n, depending on the lubricating fluid.

In the absence of water (Figure 6a), the friction coefficient calculated using the Amontons' equation is higher for diamond–quartz (μ = 0.90) than diamond–calcite (μ = 0.29). This is the opposite trend observed experimentally using humid air and aqueous environments (Figure 4). For the dry diamond–quartz contact, the linear fit through the data has an intercept close to zero. For the dry diamond–calcite contact, the linear fit to the data has a positive intercept, which suggests that there is some adhesion between the tip and the substrate.[3] This could explain why in both the current (Figure S1) and previous[37] tribometer experiments using calcite-containing rocks, carbonate material strongly adhered to the diamond surfaces. When a water monolayer is added between the tip and the substrate (Figure 6b), the friction coefficient of the diamond–quartz contact decreases significantly (μ = 0.33), while that for diamond–calcite increases (μ = 0.54). When excess water molecules are added such that the tip is submerged during sliding (Figure 6c), the friction coefficient of the diamond–quartz system decreases further (μ = 0.22), while that for diamond–calcite increases slightly (μ = 0.58). It should be noted that the increase in friction coefficient for diamond–calcite from 50 to 150 molecules is mostly due to a decrease in friction force at low load (F_n < 25 nN), since the friction forces at higher load remain identical within statistical uncertainty. The intercept of the linear fits to the diamond–calcite data decreases from 9 nN for the dry case (Figure 6a) to 2 nN when 50 water molecules are present and is negligible when 150 water molecules are added. Additional simulations suggest that there is no measurable change to the friction coefficient when further water molecules (250) are added to either system. Previous experiments have shown that the friction of granite,[92] quartzite,[92] silicon[97] and nanocrystalline diamond[98] surfaces all decrease with increased relative humidity. First-principles NEMD simulations have also shown that the presence of water molecules at the silica–silica interface significantly reduces friction by suppressing interfacial bond formation.[99] An increase in friction

in the presence of water, as observed for the diamond–calcite contact, has also been observed for some other materials, such as silicon carbide.[100] The friction coefficients from the water-containing NEMD simulations (Figure 6b and Figure 6c) are in qualitative agreement with those obtained experimentally in an air environment (Figure 4). Most importantly, the friction coefficient is much higher for the diamond–calcite than the diamond–quartz contacts.

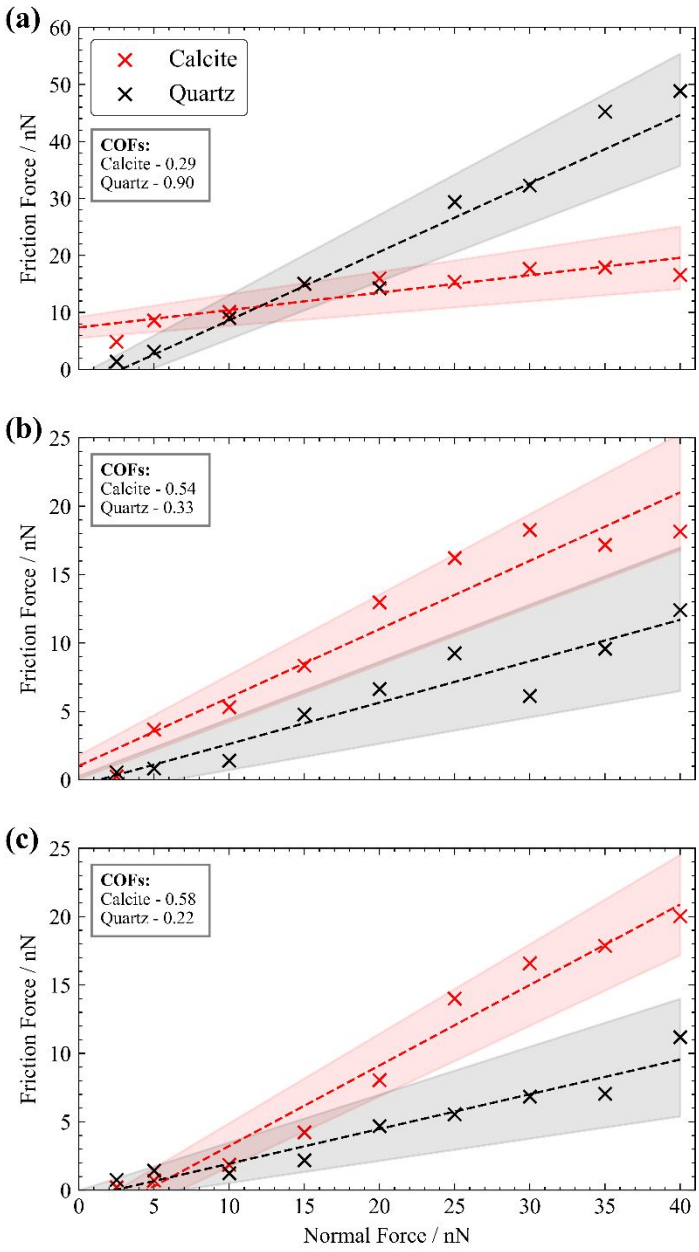

Figure 6. Variation in the friction force, F_f, with normal force, F_n, from the NEMD simulations with diamond–quartz (black) and diamond–calcite (red) point contacts with 0 (a), 50 (b), and 150 (c) water molecules. Mean forces calculated during the final 200 ps of sliding. Dashed lines are fits to Amontons' friction equation. Shaded areas represent 95 % confidence intervals.

The indentation depths in both the tribometer experiments and NEMD simulations were minimised to ensure that friction was dominated by interfacial interactions rather than ploughing. The verify that this was the case, the change in indentation depth with sliding time (Figure S6) was monitored during the NEMD simulations.[101] The indentation depth is always deeper for calcite than quartz (Figure S7), as expected due to the lower average hardness of the former (~2 GPa) compared to the latter (~15 GPa).[102] Through the purely geometrical arguments proposed by Bowden and Tabor,[103] higher friction coefficients are expected at deeper indentation depths because of a larger ploughing contribution. By comparing the how the load-dependant friction coefficient changes with indentation depth compared to the Bowden-Tabor prediction (Figure S8),[103] it is clear that the ploughing contribution is relatively small for both diamond–quartz and diamond–calcite contacts. Moreover, the large differences in the friction coefficients for diamond–quartz and diamond–calcite interfaces (Figure 6) cannot be explained through ploughing.

To understand the higher friction at the diamond–calcite interface than the diamond–quartz interface observed experimentally and in the water-containing NEMD simulations, the interfacial bond formation during sliding was quantified. The time evolutions of the interfacial bonding for the different systems and conditions are shown in Figure 7. Interfacial bonds are continuously formed and broken during sliding. As interfacial bonds break, the force on the remaining ones increases and the bond rupture becomes synchronised.[2] This cooperative rupture causes the stick-slip behaviour in the friction force observed in Figure 5. The oscillations in the friction force (Figure 5) are more pronounced than for the interfacial bonds (Figure 7). This suggests that the cooperative formation and rupture of the interfacial bonds are spatially localised at the leading and trailing edge of the tips respectively.[101] Since the formation and breaking are not temporally synchronised, there are only small fluctuations in the average number of interfacial bonds during sliding.

In the absence of water molecules, more interfacial bonds form for diamond–quartz (Figure 7b) than for diamond–calcite (Figure 7a), leading to higher friction forces and more pronounced stick-slip for the former (Figure 6). When water molecules are added at the interface, far fewer bonds form for diamond–quartz contacts (Figures 7d and 7f), while the number of bonds for diamond–calcite (Figures 7c and 7e) remains similar to the dry case. In fact, at high load (≥ 25 nN), more diamond–quartz interfacial bonds are formed when water molecules are present (Figure 7c) than when they are absent (Figure 7a). This observation could explain why the friction coefficient decreases significantly moving from 0 (Figure 6a) to 50 (Figure 6b) and 150 (Figure 6c) water molecules for diamond–quartz contacts, but increases for diamond–calcite. The larger number of interfacial bonds formed for diamond–

calcite contacts than for diamond–quartz when water is present could also explain the higher friction coefficient observed for the former in the NEMD simulations (Figure 6c) and tribometer experiments (Figure 4). Previous NEMD simulations using ReaxFF have shown that, at the interface between hydroxylated amorphous silica and oxidized silicon, the degree of atom transfer was substantially reduced when there were sufficient water molecules present to form a complete monolayer.[104] This was because the silicon atoms at the sliding interface became terminated with hydroxyl groups rather than forming interfacial bonds.[104] NEMD simulations with ReaxFF have also shown that the friction of silica surfaces reduces with increasing hydroxyl group density.[105] Similarly, experiments and first-principles calculations diamond indicated that friction generally decreases with increased relative humidity due to hydrogenation and hydroxylation that passivate the surface.[98]

Figure 7 shows that interfacial bonding increases with sliding time, reaching a steady state after around 500 ps. More interfacial bonds form and the rate of interfacial bond formation increases when the load is increased. This implies that interfacial bond formation at diamond–rock interfaces is a stress-assisted, thermally activated (SATA) process.[106] To confirm this, the temperature-dependence of the interfacial bond formation rate will be investigated in a separate study. In SATA processes, the activation energy (E_0) barrier, which determines the rates and reaction pathways, is reduced by the application of stress, such that:

$$k = Ae^{-(E_0 - N\,\sigma\,\Delta v)/(RT)} \quad (3)$$

where A is a prefactor, E_0 is the activation energy, N is Avogadro's number, σ is the applied stress, Δv the activation volume, R the universal gas constant, and T is the absolute temperature.[106] This equation predicts exponential growth in the rate with both temperature and applied stress.[106] The most appropriate stress component in Equation 3 has been debated for different systems. For the mechanochemical decomposition of lubricant additives, it has been proven that, at the macroscale, the shear stress, rather than the normal stress, is the most important parameter.[107] The shear stress has also been selected in nanoscale wear studies.[108] In most previous studies, however, the normal stress is used since this is much easier to measure and control.[106] The stress dependence of the rate of interfacial bond formation can be used to determine the activation volume, Δv.[109] The wear of silicon AFM tips on diamond surfaces[110] and the nano-manufacturing of silicon surfaces with a silica tip[111] have been shown to be SATA processes.[106] Interfacial bonding is also commonly treated as a SATA process.[93,94]

For single-asperity Hertz contacts, the contact area, A_c, is expected to increase with load as $A_c \propto F_N^{2/3}$, although previous NEMD simulations have suggested that the real contact area, $A_{real} \propto F_N$.[3] A higher contact area means that more atoms are close enough to participate in interfacial bonding. Some previous single-asperity studies of SATA processes have normalized the reaction rates by the number of atoms in contact,[110] while others have not.[111] The rates of interfacial bond formation are calculated over the first 200 ps of sliding (dotted lines in Figure 7), where the indentation depth (and thus contact area) is very similar for all of the systems and conditions studied (Figure S6). Moreover, during steady-state, the variation in contact area with load sliding is much smaller than that predicted using the Hertz equation for both diamond–quartz and diamond–calcite contacts (Figure S9). This is because micro-hardness values used in the Hertz calculations,[102] whereas the indentation depths in the NEMD simulations are always less than 0.5 nm (Figure S7). It is known for many materials that hardness decreases markedly with increasing indentation depth over the first few nanometres.[112] For these reasons, we do not normalise the rates shown in Figure 8 by the contact area.

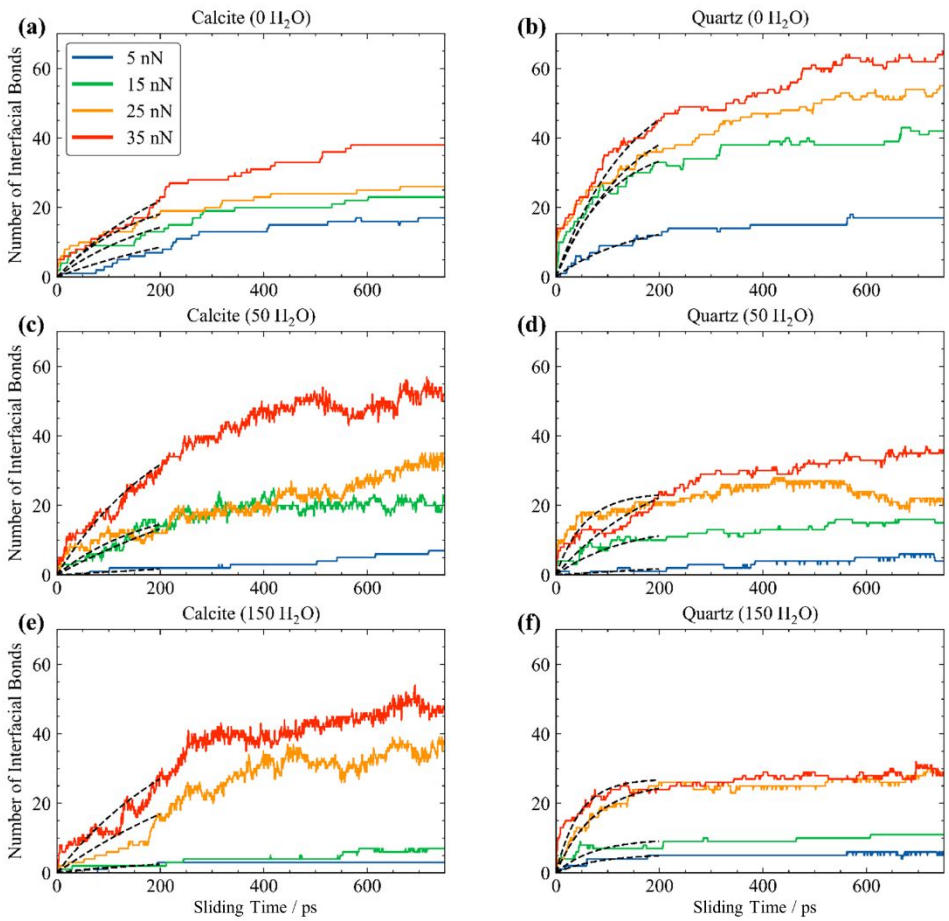

Figure 7. Variation in the total number of interfacial bonds between the tip and the surface during sliding for: (a) diamond–calcite with 0 water molecules, (b) diamond–quartz with 0 water

molecules, (c) diamond–calcite with 50 water molecules, (d) diamond–quartz with 50 water molecules, (e) diamond–calcite with 150 water molecules, and (f) diamond–quartz with 150 water molecules. Dashed lines are fits to the function ($1 - e^{-r\,t}$) over the first 200 ps, where r is the rate of interfacial bond formation and t is sliding time.[109]

Figure 8 shows how the rate of interfacial bond formation varies with applied pressure. The rates are calculated using the fits shown in Figure 7. In all cases, the rate of interfacial bond formation increases exponentially with pressure, as predicted using SATA models.[106] This observation is consistent with previous experiments and NEMD simulations of dry silica–silica contacts.[113] When no water molecules are present (Figure 8a), the rate is higher for diamond–quartz than for diamond–calcite. The slope of the linear increase in ln(rate) with pressure, which is steeper for diamond–quartz than for diamond–calcite, yields an activation volume of 1.17 ± 0.09 Å^3 for the former and 0.59 ± 0.11 Å^3 for the latter. These values are consistent with single-atom dimensions.[110] When 50 water molecules are present (Figure 8b), the rates and activation volumes are similar for both diamond–quartz and diamond–calcite, 1.33 ± 0.09 Å^3 and 1.42 ± 0.07 Å^3, respectively. This corresponds to the number of water molecules where the friction coefficients are most similar for the two substrates in Figure 4. When 150 water molecules are present at the interface (Figure 8c), the activation volume is somewhat higher for diamond–calcite (1.84 ± 0.02 Å^3) than diamond–quartz (1.26 ± 0.07 Å^3). This implies a greater stress-dependence of the rate of interfacial bond formation for wet diamond–calcite contacts than for diamond–quartz. The maximum Hertz pressure above which the rate of interfacial bonding accelerates exponentially in the NEMD simulations (2 GPa), corresponds to the pressure at F_f begins to increase superlinearly in with F_n in the macroscale experiments (Figure 4), which supports the proposed link between the two phenomena.[93]

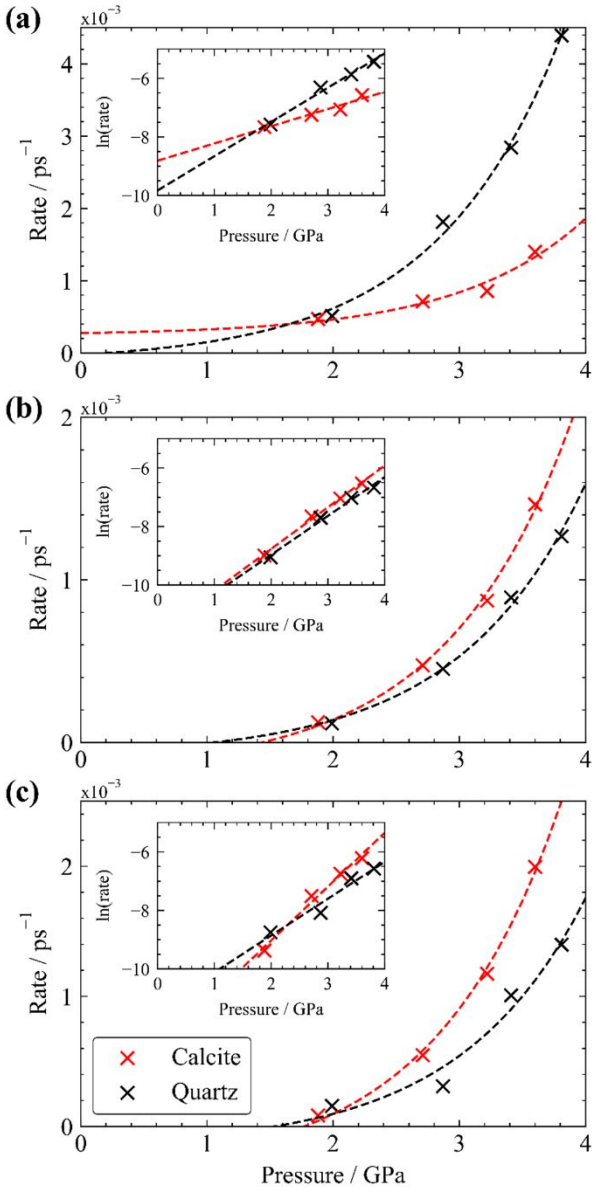

Figure 8. Variation in rate of interfacial bond formation as sliding commences with maximum Hertz pressure for: (a) 0 water molecules, 50 water molecules, 150 water molecules. Insets show linear increase in ln(rate) with pressure. Dashed lines are fits to Equation 3 used for the calculation of the activation volume.

Figure 9 shows the variation in the steady state number of interfacial bonds with load for the different systems studied. At a nanoscale, friction is proportional to the number of the interatomic interactions between the two sliding surfaces.[3] Negligible covalent bonding occurs between C atoms in the tip and Ca, C, (calcite) or Si (quartz) atoms in the substrates; however several C–O interfacial bonds are formed. In the absence of water molecules, only C–O bonds form across the interface for both diamond–calcite (Figure 9a) and diamond–quartz (Figure 9b). A greater number of interfacial C–O bonds are formed for quartz than calcite, which causes the higher friction (Figure 6). Previous NEMD simulations of dry silica–silica interfaces

using ReaxFF have shown that a larger number of interfacial bonds resulted in higher friction.[47] The force needed to break a given type of interfacial bond does not have a fixed value; it depends on the thermal state of the system and the rate at which the force is transmitted to the bond.[114]

When water is introduced at the diamond–calcite interface (Figure 9c and Figure 9e), the number of interfacial C–O bonds decreases; however, many C–O–Ca and C–H–O bridging bonds are formed. The C–O–Ca bridging bonds will be much stronger than the C–H–O hydrogen bonds.[115] Although they are relatively weak, interfacial hydrogen bonds have been shown previously to enhance friction in water-lubricated silicon carbide contacts.[100] At low load (F_n < 25 nN), the total number of interfacial bonds remains similar to the dry case for diamond–calcite. At higher load (F_n ≥ 25 nN), the number of interfacial bonds is higher when water molecules are present at the interface. For diamond–quartz, interfacial C–O bonding substantially reduces when water is added (Figure 9d and Figure 9f) and while some C–O–Si and C–H–O bonds form, the overall number of interfacial bonds is always lower than for the dry case. The percentage of intact water molecules was also monitored during the NEMD simulations. The number of intact water molecules decreases much faster at higher load (Figure S1), suggesting that this could also be a SATA process.[106] Water dissociation occurs faster and to a greater degree at the diamond–calcite interface than diamond–quartz. This dissociation facilitates a greater degree of interfacial bond formation through the O and H atoms at diamond–calcite interfaces than diamond–calcite without over-coordination of the O atoms.

Previous ReaxFF[65] NEMD and first-principles[99] NEMD simulations of aqueous silica–silica contacts showed that interfacial Si–O bonds formed during sliding at high pressure, leading to increased friction. DFTB simulations of the dry diamond–silica interface have shown that both interfacial C–O and C–Si bonds form at very high pressure (5 GPa) and sliding velocity (100 m s^{-1}).[116] Furthermore, MD simulations with ReaxFF suggested that C–Si bonding occurs at the interface between a silicon tip and a partially hydrogenated diamond substrate at high pressure.[117] Accompanying transmission electron microscopy (TEM) experiments showed that adhesion at the diamond–silicon interface increased with sliding speed and applied normal stress because these variables increased the number of bonds formed,[117] as predicted by the SATA model.[106]

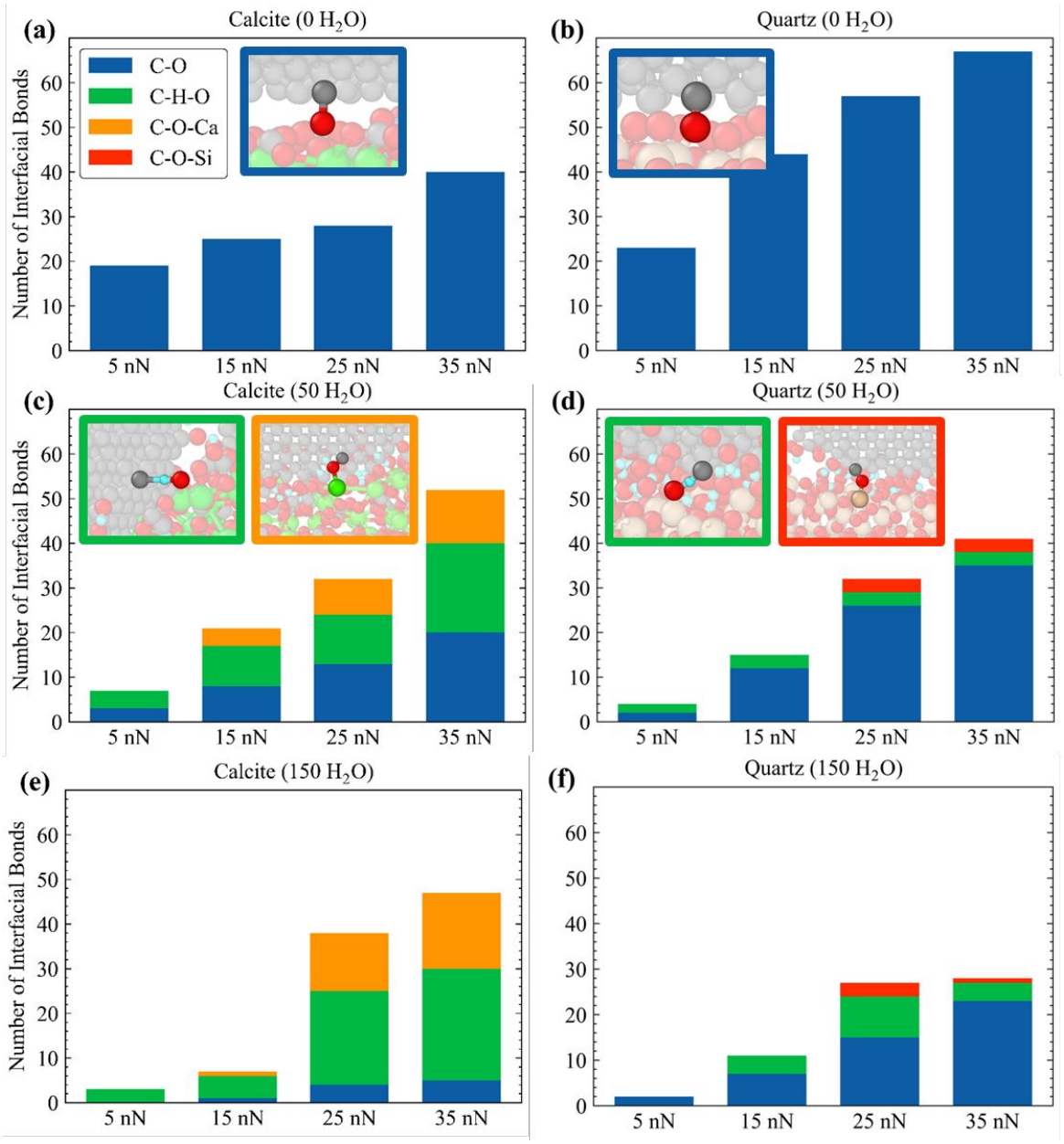

Figure 9. Type of interfacial bonds between the tip and the surface during steady-state sliding for: (a) diamond–calcite with 0 water molecules, (b) diamond–quartz with 0 water molecules, (c) diamond–calcite with 50 water molecules, (d) diamond–quartz with 50 water molecules, (e) diamond–calcite with 150 water molecules, and (f) diamond–quartz with 150 water molecules. Snapshots of each bond type are shown in the coloured boxes. Calcium atoms are shown in green, silicon in orange, carbon in grey, oxygen in red, and hydrogen in light blue. Rendered using OVITO.[67]

As a final confirmation of our hypothesis that interfacial bonding controls friction at aqueous diamond–rock interfaces, the mean number of interfacial bonding was correlated with the mean friction force for the different systems and conditions studied. Figure 10 shows that, for the water-containing systems, the mean friction force increases approximately linearly with

the mean number of interfacial bonds for both diamond–calcite and diamond–quartz contacts. This observation is consistent with both the friction model due to Filippov et al.[2] and the NEMD simulation results of Mo et al.[3], where the same relationship was observed for hydrogen-terminated amorphous carbon–diamond contacts. The gradient is steeper for diamond–calcite (Figure 10a) compared to diamond–quartz (Figure 10b), suggesting that the interfacial bonds are stronger and thus require more mechanical energy to break in the former case. The observation of superlinear friction–load behaviour in both the tribometer experiments (Figure 4) and NEMD simulations (Figure 6) suggest that interfacial bonding could also control friction in these systems not only at the nanoscale, but also at the macroscale.[93]

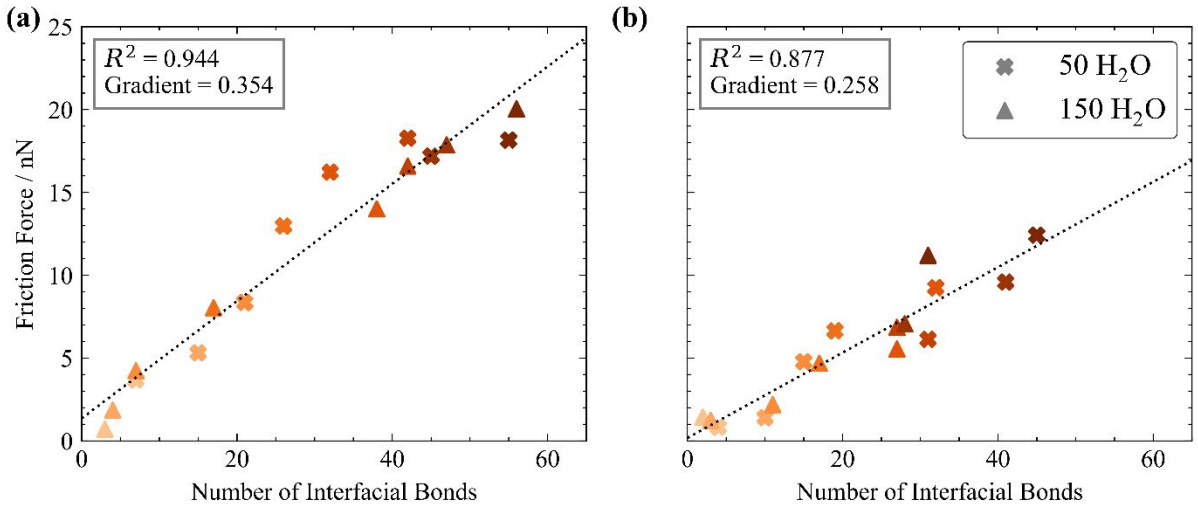

Figure 10. Correlation between the mean friction force and the mean number of interfacial bonds during steady-state sliding for diamond–calcite (a) and diamond–quartz (b). Crosses represent systems with 50 water molecules, triangles are 150 molecules, darker colours indicate higher loads.

Conclusions

In this study, macroscale tribometer experiments and NEMD simulations using ReaxFF have revealed why the friction of diamond–rock interfaces varies significantly depending on the rock type and the presence of water. Superlinear friction–load behavior is observed above a threshold pressure (2 GPa) in both the tribometer experiments in a humid air environment and NEMD simulations with water molecules present at the interface. The NEMD simulations show that this is due to interfacial bonding. The rate of interfacial bond formation increases exponentially with pressure, which is indicative of a SATA process. When water is present, the friction coefficient for diamond–calcite is much higher than for diamond–quartz in both the experiments and NEMD simulations. The NEMD simulations indicate that the higher friction coefficient for diamond–calcite than diamond–quartz contacts is due to a greater amount of

interfacial bonding. Finally, we show that the mean friction force is linearly dependant on the mean number of interfacial bonds during steady-state sliding. We expect that these findings will be useful to design new drill bit materials and coatings that minimise bit–rock interfacial bonding and thus friction.

Acknowledgements

J.S.B. thanks Baker Hughes for PhD funding. J.P.E. thanks the Royal Academy of Engineering for a Research Fellowship. D.D. and J.P.E. thank the Engineering and Physical Sciences Research Council (EPSRC) for an Established Career Fellowship EP/N025954/1 and grant EP/P030211/1. C.A.L. thanks the EPSRC and Afton Chemical Corporation for Ph.D. funding via the Theory and Simulation of Materials-Centre for Doctoral Training (TSM-CDT) EP/L015579/1. J.S.B., J.P.E., C.A.L., and D.D. acknowledge the use of the Research Computing Service at Imperial College London (DOI: 10.14469/hpc/2232) and the UK Materials and Molecular Modelling Hub, which is partially funded by EPSRC grant EP/P020194/1 and EP/T022213/1. N.D. and A.C.T.D. were supported by Multi-Scale Fluid-Solid Interactions in Architected and Natural Materials (MUSE), an Energy Frontier Research Center funded by the U.S. Department of Energy, Office of Energy Efficiency and Renewable Energy under the Basic Energy Sciences Program, Award # DE-SC0019285. The experimental data used in this study (J.A.R.B. and M.W.B.) are based upon work supported by the U.S. Department of Energy, Office of Energy Efficiency and Renewable Energy under the Geothermal Program, Award # DE-AC02-06CH11357, in partnership with Argonne National Laboratory under contract number 9F-60149. We thank Chengjiao Yu (Baker Hughes) for assistance with the tribology experiments and Julian D. Gale (Curtin University) for useful discussions on the MD simulations. All data reported in the manuscript can be obtained by emailing the corresponding author or tribology@imperial.ac.uk.

Supporting Information

Additional figures showing: surface analysis following the friction measurements (Figure S1), water dissociation (Figure S2), comparison of vibrational frequencies of $CaCO_3$ from ReaxFF and DFT (Figure S3 and Figure S4), the variation in friction force with sliding distance at different sliding velocities (Figure S5), indentation depth with sliding time (Figure S6), steady-state indentation depth with load (Figure S7), ploughing contribution to the friction coefficient (Figure 8), and change in contact area with load (Figure S9). Comparisons of heat of formation and heat of reaction of $CaCO_3$ (Table S1). ReaxFF parameters for $CaCO_3$.

References

(1) Vanossi, A.; Manini, N.; Urbakh, M.; Zapperi, S.; Tosatti, E. Colloquium: Modeling Friction: From Nanoscale to Mesoscale. *Rev. Mod. Phys.* **2013**, *85*, 529–552.

(2) Filippov, A. E.; Klafter, J.; Urbakh, M. Friction through Dynamical Formation and Rupture of Molecular Bonds. *Phys. Rev. Lett.* **2004**, *92*, 135503.

(3) Mo, Y.; Turner, K. T.; Szlufarska, I. Friction Laws at the Nanoscale. *Nature* **2009**, *457*, 1116–1119.

(4) Li, Q.; Tullis, T. E.; Goldsby, D.; Carpick, R. W. Frictional Ageing from Interfacial Bonding and the Origins of Rate and State Friction. *Nature* **2011**, *480*, 233–236.

(5) Dieterich, J. H. Time-Dependent Friction in Rocks. *J. Geophys. Res.* **1972**, *77*, 3690–3697.

(6) Cleveland, C. J. Net Energy from the Extraction of Oil and Gas in the United States. *Energy* **2005**, *30*, 769–782.

(7) Moore, J. N.; Simmons, S. F. More Power from Below. *Science.* **2013**, *340*, 933–934.

(8) Bui, M.; Adjiman, C. S.; Bardow, A.; Anthony, E. J.; Boston, A.; Brown, S.; Fennell, P. S.; Fuss, S.; Galindo, A.; Hacket, L. A.; et al. Carbon Capture and Storage (CCS): The Way Forward. *Energy Environ. Sci.* **2018**, *11*, 1062–1176.

(9) Krall, L.; McCartin, T.; MacFarlane, A. Siting Deep Boreholes for Disposal of Radioactive Waste: Consequences for Tight Coupling between Natural and Engineered Systems. *Environ. Sci. Technol.* **2020**, *54*, 629–646.

(10) Holmberg, K.; Erdemir, A. Influence of Tribology on Global Energy Consumption, Costs and Emissions. *Friction* **2017**, *5*, 263–284.

(11) Teale, R. The Concept of Specific Energy in Rock Drilling. *Int. J. Rock Mech. Min. Sci.* **1965**, *2*, 57–73.

(12) Zhou, Y.; Zhang, W.; Gamwo, I.; Lin, J. S. Mechanical Specific Energy versus Depth of Cut in Rock Cutting and Drilling. *Int. J. Rock Mech. Min. Sci.* **2017**, *100*, 287–297.

(13) Perrott, C. M. Tool Materials for Drilling and Mining. *Ann. Rev. Mater. Sci.* **1979**, *9*, 23–50.

(14) Lukawski, M. Z.; Anderson, B. J.; Augustine, C.; Capuano, L. E.; Beckers, K. F.; Livesay, B.; Tester, J. W. Cost Analysis of Oil, Gas, and Geothermal Well Drilling. *J. Pet. Sci. Eng.* **2014**, *118*, 1–14.

(15) Lyons, K. D.; Honeygan, S.; Mroz, T. NETL Extreme Drilling Laboratory Studies High Pressure High Temperature Drilling Phenomena. *J. Energy Resour. Technol.* **2008**, *130*, 0431021.

(16) Wentorf, R. H.; DeVries, R. C.; Bundy, F. P. Sintered Superhard Materials. *Science.* **1980**, *208*, 873–880.

(17) Appl, F. C.; Wilson, C. C.; Lakshman, I. Measurement of Forces, Temperatures and Wear of PDC Cutters in Rock Cutting. *Wear* **1993**, *169*, 9–24.

(18) Pessier, R. C.; Fear, M. J. Quantifying Common Drilling Problems with Mechanical Specific Energy and a Bit-Specific Coefficient of Sliding Friction. In *SPE Annual Technical Conference and Exhibition*; Society of Petroleum Engineers: Washington D.C., 1992; p SPE-24584.

(19) Wheeler, D. W. Applications of Diamond to Improve Tribological Performance in the Oil and Gas Industry. *Lubricants* **2018**, *6*, 84.

(20) Glowka, D. A. The Thermal Response of Rock to Friction in the Drag Cutting Process. *J. Struct. Geol.* **1989**, *11*, 919–931.

(21) Mehan, R. L.; Hibbs, L. E. Thermal Degradation of Sintered Diamond Compacts. *J. Mater. Sci.* **1989**, *24*, 942–950.

(22) Burwell, J. T. Survey of Possible Wear Mechanisms. *Wear* **1957**, *1*, 119–141.

(23) Ersoy, A.; Waller, M. D. Wear Characteristics of PDC Pin and Hybrid Core Bits in Rock Drilling. *Wear* **1995**, *188*, 150–165.

(24) Archard, J. F. Contact and Rubbing of Flat Surfaces. *J. Appl. Phys.* **1953**, *24*, 981.

(25) Kauzlarich, J. J.; Williams, J. A. Archard Wear and Component Geometry. *Proc. Inst. Mech. Eng. Part J* **2001**, *215*, 387–398.

(26) Yahiaoui, M.; Gerbaud, L.; Paris, J.-Y.; Denape, J.; Dourfaye, A. A Study on PDC Drill Bits Quality. *Wear* **2013**, *298–299*, 32–41.

(27) Yahiaoui, M.; Paris, J.-Y.; Delbé, K.; Denape, J.; Gerbaud, L.; Colin, C.; Ther, O.; Dourfaye, A. Quality and Wear Behavior of Graded Polycrystalline Diamond Compact Cutters. *Int. J. Refract. Met. Hard Mater.* **2016**, *56*, 87–95.

(28) Wang, C.; Li, S.; Zhang, L. Evaluation of Rock Abrasiveness Class Based on the Wear Mechanisms of PDC Cutters. *J. Pet. Sci. Eng.* **2019**, *174*, 959–967.

(29) Beste, U.; Lundvall, A.; Jacobson, S. Micro-Scratch Evaluation of Rock Types - A Means to Comprehend Rock Drill Wear. *Tribol. Int.* **2004**, *37*, 203–210.

(30) Bex, P. A.; Shafto, G. R. The Influence of Temperature and Heating Time on PCD Performance. *Ind. Diam. Div. Commun.* **1978**, *44*, 128–132.

(31) Rabinowicz, E. Abrasive Wear Resistance as a Materials Test. *Lubr. Eng.* **1977**, *33*, 378–381.

(32) Urbakh, M.; Klafter, J.; Gourdon, D.; Israelachvili, J. The Nonlinear Nature of Friction. *Nature* **2004**, *430*, 525–528.

(33) Richard, T.; Germay, C.; Detournay, E. A Simplified Model to Explore the Root Cause of Stick-Slip Vibrations in Drilling Systems with Drag Bits. *J. Sound Vib.* **2007**, *305*, 432–456.

(34) Kovalyshen, Y. Understanding Root Cause of Stick-Slip Vibrations in Deep Drilling

with Drag Bits. *Int. J. Non. Linear. Mech.* **2015**, *67*, 331–341.

(35) Chen, S.; Wisinger, J.; Dunbar, B.; Propes, C. Identification and Mitigation of Friction-And Cutting Action-Induced Stick-Slip Vibrations with PDC Bits. *SPE Drill. Complet.* **2020**, *35*, 576–587.

(36) Carpenter, C. Resolving Torsional Vibration in Limestone Reservoirs Reduces Equipment Damage. *J. Pet. Technol.* **2019**, *71*, 68–69.

(37) Dagrain, F.; Richard, T. On the Influence of PDC Wear and Rock Type on Friction Coefficient and Cutting Efficiency. In *Eurock 2006: Multiphysics Coupling and Long Term Behaviour in Rock Mechanics*; Liege, Belgium, 2006; pp 577–584.

(38) Tian, K.; Gosvami, N. N.; Goldsby, D. L.; Carpick, R. W. Stick-Slip Instabilities for Interfacial Chemical Bond-Induced Friction at the Nanoscale. *J. Phys. Chem. B* **2018**, *122*, 991–999.

(39) Rehbinder, P. A.; Shchukin, E. D. Surface Phenomena in Solids during Deformation and Fracture Processes. *Prog. Surf. Sci.* **1972**, *3*, 97–187.

(40) Westwood, A. R. C.; Ahearn, J. S.; Mills, J. J. Developments in the Theory and Application of Chemomechanical Effects. *Colloids Surf.* **1981**, *2*, 1–35.

(41) Mills, J. J.; Westwood, A. R. C. Influence of Chemomechanically Active Fluids on Diamond Wear during Hard Rock Drilling. *J. Mater. Sci.* **1978**, *13*, 2712–2716.

(42) Mills, J. J.; Westwood, A. R. C. Influence of Adsorption Kinetics on Chemomechanically Enhanced Hard Rock Drilling. *J. Mater. Sci.* **1980**, *15*, 3010–3016.

(43) Cooper, G.; Berlie, J. On the Influence of the Flushing Fluid during Diamond Drilling. *J. Mater. Sci.* **1976**, *11*, 1771–1775.

(44) Menezes, P. L.; Lovell, M. R.; Avdeev, I. V.; Higgs III, C. F. Studies on the Formation of Discontinuous Rock Fragments during Cutting Operation. *Int. J. Rock Mech. Min. Sci.* **2014**, *71*, 131–142.

(45) Cheng, Z.; Li, G.; Huang, Z.; Sheng, M.; Wu, X.; Yang, J. Analytical Modelling of Rock Cutting Force and Failure Surface in Linear Cutting Test by Single PDC Cutter. *J. Pet. Sci. Eng.* **2019**, *177*, 306–316.

(46) Ewen, J. P.; Heyes, D. M.; Dini, D. Advances in Nonequilibrium Molecular Dynamics Simulations of Lubricants and Additives. *Friction* **2018**, *6*, 349–386.

(47) Li, A.; Liu, Y.; Szlufarska, I. Effects of Interfacial Bonding on Friction and Wear at Silica/Silica Interfaces. *Tribol. Lett.* **2014**, *56*, 481–490.

(48) Wang, Y.; Xu, J.; Ootani, Y.; Bai, S.; Higuchi, Y.; Ozawa, N.; Adachi, K.; Martin, J. M.; Kubo, M. Tight-Binding Quantum Chemical Molecular Dynamics Study on the Friction and Wear Processes of Diamond-Like Carbon Coatings: Effect of Tensile Stress. *ACS Appl. Mater. Interfaces* **2017**, *9*, 34396–34404.

(49) van Duin, A. C. T.; Dasgupta, S.; Lorant, F.; Goddard III, W. A. ReaxFF: A Reactive Force Field for Hydrocarbons. *J. Phys. Chem. A* **2001**, *105*, 9396–9409.

(50) Plimpton, S. J.; Thompson, A. P. Computational Aspects of Many-Body Potentials. *MRS Bull.* **2012**, *37*, 513–521.

(51) Senftle, T. P.; Hong, S.; Islam, M. M.; Kylasa, S. B.; Zheng, Y.; Shin, Y. K.; Junkermeier, C.; Engel-Herbert, R.; Janik, M. J.; Aktulga, H. M.; et al. The ReaxFF Reactive Force-Field: Development, Applications and Future Directions. *npj Comput. Mater.* **2016**, *2*, 15011.

(52) Martini, A.; Eder, S. J.; Dörr, N. Tribochemistry: A Review of Reactive Molecular Dynamics Simulations. *Lubricants* **2020**, *8*, 44.

(53) Newsome, D. A.; Sengupta, D.; Foroutan, H.; Russo, M. F.; Van Duin, A. C. T. Oxidation of Silicon Carbide by O2 and H2O: A ReaxFF Reactive Molecular Dynamics Study, Part I. *J. Phys. Chem. C* **2012**, *116*, 16111–16121.

(54) Dougherty, P. S. M.; Pudjoprawoto, R.; Higgs III, C. F. Bit Cutter-on-Rock Tribometry: Analyzing Friction and Rate-of-Penetration for Deep Well Drilling Substrates. *Tribol. Int.* **2014**, *77*, 178–185.

(55) Reeves, M. J. Rock Surface Roughness and Frictional Strength. *Int. J. Rock Mech. Min. Sci.* **1985**, *22*, 429–442.

(56) Greenwood, J. A.; Johnson, K. L.; Matsubara, E. A Surface Roughness Parameter in Hertz Contact. *Wear* **1984**, *100*, 47–57.

(57) Lai, P.; Moulton, K.; Krevor, S. Pore-Scale Heterogeneity in the Mineral Distribution and Reactive Surface Area of Porous Rocks. *Chem. Geol.* **2015**, *411*, 260–273.

(58) Van der Molen, I. The Shift of the α-β Transition Temperature of Quartz Associated with the Thermal Expansion of Granite at High Pressure. *Tectonophysics* **1981**, *73*, 323–342.

(59) Levenson, Y.; Emmanuel, S. Pore-Scale Heterogeneous Reaction Rates on a Dissolving Limestone Surface. *Geochim. Cosmochim. Acta* **2013**, *119*, 188–197.

(60) De Leeuw, N. H.; Higgins, F. M.; Parker, S. C. Modeling the Surface Structure and Stability of α-Quartz. *J. Phys. Chem. B* **1999**, *103*, 1270–1277.

(61) Kerisit, S.; Parker, S. C.; Harding, J. H. Atomistic Simulation of the Dissociative Adsorption of Water on Calcite Surfaces. *J. Phys. Chem. B* **2003**, *107*, 7676–7682.

(62) Pashley, R. M.; Kitchener, J. A. Surface Forces in Adsorbed Multilayers of Water on Quartz. *J. Colloid Interface Sci.* **1979**, *71*, 491–500.

(63) Stipp, S. L. S.; Hochella, M. F. Structure and Bonding at the Calcite Surface as Observed with X-Ray Photoelectron Spectroscopy (XPS) and (LEED). *Geochim. Cosmochim. Acta* **1991**, *55*, 1723–1736.

(64) Yang, J.; Wang, E. G. Water Adsorption on Hydroxylated α-Quartz (0001) Surfaces:

From Monomer to Flat Bilayer. *Phys. Rev. B* **2006**, *73*, 035406.

(65) Yue, D. C.; Ma, T. B.; Hu, Y. Z.; Yeon, J.; van Duin, A. C. T.; Wang, H.; Luo, J. Tribochemical Mechanism of Amorphous Silica Asperities in Aqueous Environment: A Reactive Molecular Dynamics Study. *Langmuir* **2015**, *31*, 1429–1436.

(66) Brazil, O.; Pharr, G. M. Direct Observation of Partial Slip in Micrometre-Scale Single Asperity Contacts. *Tribol. Int.* **2021**, *155*, 106776.

(67) Stukowski, A. Visualization and Analysis of Atomistic Simulation Data with OVITO-the Open Visualization Tool. *Model. Simul. Mater. Sci. Eng.* **2010**, *18*, 015012.

(68) Chenoweth, K.; van Duin, A. C. T.; Goddard III, W. A. ReaxFF Reactive Force Field for Molecular Dynamics Simulations of Hydrocarbon Oxidation. *J. Phys. Chem. A* **2008**, *112*, 1040–1053.

(69) Aktulga, H. M.; Fogarty, J. C.; Pandit, S. A.; Grama, A. Y. Parallel Reactive Molecular Dynamics: Numerical Methods and Algorithmic Techniques. *Parallel Comput.* **2012**, *38*, 245–259.

(70) Rappe, A. K.; Goddard III, W. A. Charge Equilibration for Molecular Dynamics Simulations. *J. Phys. Chem.* **1991**, *95*, 3358–3363.

(71) Nakano, A. Parallel Multilevel Preconditioned Conjugate-Gradient Approach to Variable-Charge Molecular Dynamics. *Comput. Phys. Commun.* **1997**, *104*, 59–69.

(72) Buehler, M. J.; van Duin, A. C. T.; Goddard III, W. A. Multiparadigm Modeling of Dynamical Crack Propagation in Silicon Using a Reactive Force Field. *Phys. Rev. Lett.* **2006**, *96*, 095505.

(73) van Duin, A. C. T.; Strachan, A.; Stewman, S.; Zhang, Q.; Xu, X.; Goddard III, W. A. ReaxFFSiO Reactive Force Field for Silicon and Silicon Oxide Systems. *J. Phys. Chem. A* **2003**, *107*, 3803–3811.

(74) Fogarty, J. C.; Aktulga, H. M.; Grama, A. Y.; van Duin, A. C. T.; Pandit, S. A. A Reactive Molecular Dynamics Simulation of the Silica-Water Interface. *J. Chem. Phys.* **2010**, *132*, 174704.

(75) Chenoweth, K.; Cheung, S.; van Duin, A. C. T.; Goddard III, W. A.; Kober, E. M. Simulations on the Thermal Decomposition of a Poly(Dimethylsiloxane) Polymer Using the ReaxFF Reactive Force Field. *J. Am. Chem. Soc.* **2005**, *127*, 7192–7202.

(76) Kumar, S.; Parks, D.; Kamrin, K. Mechanistic Origin of the Ultrastrong Adhesion between Graphene and A-SiO2: Beyond van Der Waals. *ACS Nano* **2016**, *10*, 6552–6562.

(77) Pitman, M. C.; van Duin, A. C. T. Dynamics of Confined Reactive Water in Smectite Clay-Zeolite Composites. *J. Am. Chem. Soc.* **2012**, *134*, 3042–3053.

(78) Manzano, H.; Pellenq, R. J. M.; Ulm, F. J.; Buehler, M. J.; van Duin, A. C. T. Hydration of Calcium Oxide Surface Predicted by Reactive Force Field Molecular

Dynamics. *Langmuir* **2012**, *28*, 4187–4197.

(79) Raiteri, P.; Demichelis, R.; Gale, J. D.; Kellermeier, M.; Gebauer, D.; Quigley, D.; Wright, L. B.; Walsh, T. R. Exploring the Influence of Organic Species on Pre- and Post-Nucleation Calcium Carbonate. *Faraday Discuss.* **2012**, *159*, 61–85.

(80) Gale, J. D.; Raiteri, P.; van Duin, A. C. T. A Reactive Force Field for Aqueous-Calcium Carbonate Systems. *Phys. Chem. Chem. Phys.* **2011**, *13*, 16666–16679.

(81) Bochevarov, A. D.; Harder, E.; Hughes, T. F.; Greenwood, J. R.; Braden, D. A.; Philipp, D. M.; Rinaldo, D.; Halls, M. D.; Zhang, J.; Friesner, R. A. Jaguar: A High-Performance Quantum Chemistry Software Program with Strengths in Life and Materials Sciences. *Int. J. Quantum Chem.* **2013**, *113*, 2110–2142.

(82) Sherrill, C. D.; Takatani, T.; Hohenstein, E. G. An Assessment of Theoretical Methods for Nonbonded Interactions: Comparison to Complete Basis Set Limit Coupled-Cluster Potential Energy Curves for the Benzene Dimer, the Methane Dimer, Benzene-Methane, and Benzene-H2S. *J. Phys. Chem. A* **2009**, *113*, 10146–10159.

(83) Kresse, G.; Hafner, J. Ab Initio Molecular Dynamics for Liquid Metals. *Phys. Rev. B* **1993**, *47*, 558.

(84) Kresse, G.; Furthmuller, J. Efficiency of Ab-Initio Total Energy Calculations for Metals and Semiconductors Using a Plane-Wave Basis Set. *Comput. Mater. Sci.* **1996**, *6*, 15–50.

(85) Kresse, G.; Furthmuller, J. Efficient Iterative Schemes for Ab Initio Total-Energy Calculations Using a Plane-Wave Basis Set. *Phys. Rev. B* **1996**, *54*, 11169.

(86) Kresse, G.; Joubert, D. From Ultrasoft Pseudopotentials to the Projector Augmented-Wave Method. *Phys. Rev. B.* **1999**, *59*, 1758–1775.

(87) Perdew, J. P.; Burke, K.; Ernzerhof, M. Generalized Gradient Approximation Made Simple. *Phys. Rev. Lett.* **1996**, *77*, 3865–3868.

(88) Monkhorst, H. J.; Pack, J. D. Special Points for Brillouin-Zone Integrations. *Phys. Rev. B* **1976**, *13*, 5188–5192.

(89) Plimpton, S. Fast Parallel Algorithms for Short-Range Molecular-Dynamics. *J. Comput. Phys.* **1995**, *117*, 1–19.

(90) Verlet, L. Computer “Experiments” on Classical Fluids. I. Thermodynamical Properties of Lennard-Jones Molecules. *Phys. Rev.* **1967**, *159*, 98.

(91) Ewen, J. P.; Ayestarán Latorre, C.; Gattinoni, C.; Khajeh, A.; Moore, J. D.; Remias, J. E.; Martini, A.; Dini, D. Substituent Effects on the Thermal Decomposition of Phosphate Esters on Ferrous Surfaces. *J. Phys. Chem. C* **2020**, *124*, 9852–9865.

(92) Dieterich, J. H.; Conrad, G. Effect of Humidity on Time- and Velocity-Dependent Friction in Rocks. *J. Geophys. Res.* **1984**, *89*, 4196–4202.

(93) Ouyang, W.; Cheng, Y.; Ma, M.; Urbakh, M. Load-Velocity-Temperature Relationship

in Frictional Response of Microscopic Contacts. *J. Mech. Phys. Solids* **2020**, *137*, 103880.

(94) Ouyang, W.; Ramakrishna, S. N.; Rossi, A.; Urbakh, M.; Spencer, N. D.; Arcifa, A. Load and Velocity Dependence of Friction Mediated by Dynamics of Interfacial Contacts. *Phys. Rev. Lett.* **2019**, *123*, 116102.

(95) Yahiaoui, M.; Paris, J.-Y.; Delbé, K.; Denape, J.; Gerbaud, L.; Dourfaye, A. Independent Analyses of Cutting and Friction Forces Applied on a Single Polycrystalline Diamond Compact Cutter. *Int. J. Rock Mech. Min. Sci.* **2016**, *85*, 20–26.

(96) Tian, K.; Gosvami, N. N.; Goldsby, D. L.; Liu, Y.; Szlufarska, I.; Carpick, R. W. Load and Time Dependence of Interfacial Chemical Bond-Induced Friction at the Nanoscale. *Phys. Rev. Lett.* **2017**, *118*, 076103.

(97) Patton, S. T.; Cowan, W. D.; Eapen, K. C.; Zabinski, J. S. Effect of Surface Chemistry on the Tribological Performance of a MEMS Electrostatic Lateral Output Motor. *Tribol. Lett.* **2001**, *9*, 199–209.

(98) De Barros Bouchet, M.-I.; Zilibotti, G.; Matta, C.; Righi, M. C.; Vandenbulcke, L.; Vacher, B.; Martin, J.-M. Friction of Diamond in the Presence of Water Vapor and Hydrogen Gas. Coupling Gas-Phase Lubrication and First-Principles Studies. *J. Phys. Chem. C* **2012**, *116*, 6966–6972.

(99) Ootani, Y.; Xu, J.; Hatano, T.; Kubo, M. Contrasting Roles of Water at Sliding Interfaces between Silicon- Based Materials: First-Principles Molecular Dynamics Sliding Simulations. *J. Phys. Chem. C* **2018**, *122*, 10459–10467.

(100) Liu, Y.; Szlufarska, I. Effect of Trace Moisture on Friction. *Appl. Phys. Lett.* **2010**, *96*, 101902.

(101) Gao, H.; Ewen, J. P.; Hartkamp, R.; Müser, M. H.; Dini, D. Scale-Dependent Friction-Coverage Relations and Nonlocal Dissipation in Surfactant Monolayers. *Langmuir* **2021**, *37*, 2406–2418.

(102) Broz, M. E.; Cook, R. F.; Whitney, D. L. Microhardness, Toughness, and Modulus of Mohs Scale Minerals. *Am. Mineral.* **2006**, *91*, 135–142.

(103) Bowden, F.; Tabor, D. Friction, Lubrication and Wear: A Survey of Work during the Last Decade. *Br. J. Appl. Phys.* **1966**, *17*, 1521–1544.

(104) Yeon, J.; van Duin, A. C. T.; Kim, S. H. Effects of Water on Tribochemical Wear of Silicon Oxide Interface: Molecular Dynamics (MD) Study with Reactive Force Field (ReaxFF). *Langmuir* **2016**, *32*, 1018–1026.

(105) Wang, M.; Duan, F.; Mu, X. Effect of Surface Silanol Groups on Friction and Wear between Amorphous Silica Surfaces. *Langmuir* **2019**, *35*, 5463–5470.

(106) Spikes, H. A. Stress-Augmented Thermal Activation: Tribology Feels the Force.

Friction **2018**, *6*, 1–31.

(107) Zhang, J.; Ewen, J. P.; Ueda, M.; Wong, J. S. S.; Spikes, H. A. Mechanochemistry of Zinc Dialkyldithiophosphate on Steel Surfaces under Elastohydrodynamic Lubrication Conditions. *ACS Appl. Mater. Interfaces* **2020**, *12*, 6662–6676.

(108) Gotsmann, B.; Lantz, M. A. Atomistic Wear in a Single Asperity Sliding Contact. *Phys. Rev. Lett.* **2008**, *101*, 125501.

(109) Yeon, J.; He, X.; Martini, A.; Kim, S. H. Mechanochemistry at Solid Surfaces: Polymerization of Adsorbed Molecules by Mechanical Shear at Tribological Interfaces. *ACS Appl. Mater. Interfaces* **2017**, *9*, 3142–3148.

(110) Jacobs, T. D. B.; Carpick, R. W. Nanoscale Wear as a Stress-Assisted Chemical Reaction. *Nat. Nanotechnol.* **2013**, *8*, 108–112.

(111) Chen, L.; Wen, J.; Zhang, P.; Yu, B.; Chen, C.; Ma, T.; Lu, X.; Kim, S. H.; Qian, L. Nanomanufacturing of Silicon Surface with a Single Atomic Layer Precision via Mechanochemical Reactions. *Nat. Commun.* **2018**, *9*, 1542.

(112) Tayebi, N.; Conry, T. F.; Polycarpou, A. A. Determination of Hardness from Nanoscratch Experiments: Corrections for Interfacial Shear Stress and Elastic Recovery. *J. Mater. Res.* **2003**, *18*, 2150–2162.

(113) Vorholzer, M.; Vilhena, J. G.; Perez, R.; Gnecco, E.; Dietzel, D.; Schirmeisen, A. Temperature Activates Contact Aging in Silica Nanocontacts. *Phys. Rev. X* **2019**, *91*, 041045.

(114) Ghatak, A.; Vorvolakos, K.; She, H.; Malotky, D. L.; Chaudhury, M. K. Interfacial Rate Processes in Adhesion and Friction. *J. Phys. Chem. B* **2000**, *104*, 4018–4030.

(115) Steiner, T. C-H···O Hydrogen Bonding in Crystals. *Crystallogr. Rev.* **2003**, *9*, 177–228.

(116) Peguiron, A.; Moras, G.; Walter, M.; Uetsuka, H.; Pastewka, L.; Moseler, M. Activation and Mechanochemical Breaking of C-C Bonds Initiate Wear of Diamond (110) Surfaces in Contact with Silica. *Carbon.* **2016**, *98*, 474–483.

(117) Milne, Z.; Schall, J. D.; Jacobs, T. D. B.; Harrison, J.; Carpick, R. W. Covalent Bonding and Atomic-Level Plasticity Increase Adhesion in Silicon-Diamond Nanocontacts. *ACS Appl. Mater. Interfaces* **2019**, *11*, 40734–40748.

TOC Graphic